



Microstructural evolution in laser melted boron alloyed Ti-6Al-4V

Huseyin Hizli^{a,b}, Zhiyi Zou^b, James Murray^a, Adam Clare^{a,c}, Marco Simonelli^{b,*}

^a Advanced Component Engineering Laboratory, Faculty of Engineering, University of Nottingham, Nottingham NG8 1BB, UK

^b Centre for Additive Manufacturing, Faculty of Engineering, University of Nottingham, Nottingham NG8 1BB, UK

^c Department of Mechanical Engineering, University of British Columbia, Vancouver Campus, 6250 Applied Science Lane, Vancouver, Canada

ARTICLE INFO

Keywords:

Titanium alloys
In-situ synthesis TiB
Microstructural evolution
Alloy design
Additive manufacturing
In-situ grain refinement

ABSTRACT

Grain refinement in cast titanium alloys has been demonstrated through the addition of boron (B) in hypoeutectic concentration. However, there is still a poor understanding of how effective B is towards microstructural refinement under rapid solidification conditions. This study investigates the impact of boron (B) addition on the microstructure formation in Ti-6Al-4 V alloys under rapid solidification conditions, particularly relevant to Laser Powder Bed Fusion (PBF-LB), a leading technique in metal additive manufacturing. By examining a range of Ti-6Al-4 V-xB alloys with boron contents varying from 0 wt% to 2.5 wt%, prepared through arc melting and subsequent laser surface melting to mimic PBF-LB conditions, our empirical analysis focuses on identifying the threshold B concentration for effective in-situ grain refinement in these alloys. Results indicate that a boron concentration of 0.2 wt% or higher significantly refines the microstructure of Ti-6Al-4 V alloy, leading to the formation of a quasi-continuous TiB network. Crucially, our comprehensive analysis across all samples reveals a consistent microstructural composition, characterized by the presence of martensitic alpha and titanium boride (TiB) phases, with an absence of the beta-titanium (β -Ti) phase. This underlines the significant role of boron in stabilizing these specific phases, thus contributing to our understanding of phase formation dynamics in boron-modified Ti-6Al-4 V alloys under rapid solidification conditions.

1. Introduction

In the past decades, additive manufacturing (AM), especially Laser Powder Bed Fusion (PBF-LB), has demonstrated its potential to revolutionise the manufacturing of metallic products [1–3]. However, when it comes to titanium products in safety-critical structural applications, processing via PBF-LB and suitable materials is still under development [4]. Ti-6Al-4 V, generally considered a reference titanium alloy, suffers from the fast-cooling rate imposed by PBF-LB, which leads to the formation of a martensitic α' microstructure [5–7], and the epitaxial growth of prior β -grains throughout the deposited layers [5,8–11]. This anisotropic microstructure with brittle martensitic phase renders a material with high strength, low ductility, high residual stresses [12], significant solidification texture [13], low fatigue resistance and poor fracture toughness.

A number of approaches have been adopted to promote the microstructure and mechanical properties of PBF-LB Ti alloys. Examples include: carefully tuning the laser parameters and scan strategies to decompose the martensitic α' [14–16] and conduction of post-process treatments to obtain a more desirable $\alpha + \beta$ microstructure [17–19].

Composition design is another widely applied approach. Altering the existing alloy elements and/or adding additional trace elements are the two popular routes to designing titanium alloy better suited for PBF-LB. Ideally, the preferred alloy elements should lead to a wide solidification temperature range and induce a large constitutional undercooling ahead of the solid/liquid interface, as it would help to form fine equiaxed grains under fast-cooling [20]. With this in mind, Nickel (Ni) [21], tungsten (W) [22], molybdenum (Mo) [23], chromium (Cr) [24], copper (Cu) [25] and iron (Fe) [26] have been reported for in-situ equiaxed grain formation in titanium alloy AM. Bermingham *et al.* estimated the growth restriction factor (Q) of different alloying elements in titanium alloy for casting application and concluded that Boron (B) has a more significant refining effect [27]. It is well established from the literature that in traditional manufacturing routes, B, with a large Q in titanium alloy, leads to significant alterations in the microstructure and corresponding mechanical properties, such as refining β -grain sizes and α -lath size [28,29]. The large constitutional undercooling, due to the inhomogeneous distribution of minor constituents at the solid/liquid interface, as the result of the rejection of B from primarily solidified grains into the liquid ahead of the solidification front, is the main reason

* Corresponding author.

E-mail address: Marco.Simonelli@nottingham.ac.uk (M. Simonelli).

<https://doi.org/10.1016/j.jalcom.2024.173762>

Received 22 November 2023; Received in revised form 15 January 2024; Accepted 1 February 2024

Available online 3 February 2024

0925-8388/© 2024 The Authors. Published by Elsevier B.V. This is an open access article under the CC BY license (<http://creativecommons.org/licenses/by/4.0/>).

behind the grain refinement [30,31].

Previous research has demonstrated that adding B to titanium alloys can effectively refine the grain structure. While most of the related research has focused on casting techniques [28,30,32,33], some have now emerged in additive manufacturing. For instance, Attar et al. [34] reported microstructural refinement in pure Ti processed by PBF-LB after adding 1.5 wt% B, although they could not quantify the extent of the refinement effect. In wire arc additive manufacturing, Birmingham et al. [20] added trace amounts of B (<0.13 wt%) and observed a reduction in the width of columnar grains and refinement in the α grain size, but they did not achieve a Columnar to Equiaxed Transition (CET). Similarly, Rahman Rashid et al. [35] added 0.04 wt% B to Ti-6Al-4 V and reported a refinement of the α grains size after single layer DLD cladding, but did not report β grain refinement. Mahbooba et al. [36] reported that B addition less than 1 wt% would not trigger CET for electron beam AM of Ti-6Al-4 V, only columnar grain narrowing can be observed.

It has been proven that trace (<0.40 wt%) B addition can considerably refine the grain structure and improve the mechanical performance of WAAM and DED Ti-6Al-4 V alloy [37–40]. Compared to these AM processes, the PBF-LB process is characterised by a much higher energy density and cooling rates, resulting in a more intense competition between epitaxial growth and nucleation in the solidifying molten pool. Currently, there is a lack of understanding of the effective amount of B addition, and how it affects the microstructural development and mechanical performance of PBF-LB Ti-6Al-4 V-xB. After reviewing the published research, we could not find any report on using B addition to trigger columnar-to-equiaxed transformation in PBF-LB Ti-6Al-4 V-xB.

To better bridge such gap in the knowledge, this work employed a powder-free approach to evaluate the microstructure in a range of Ti-6Al-4 V-xB compositions via laser irradiation of arc-melted buttons. The essence of this method assumes that a laser-deposited melt pool on the surface of a bulk alloy provides a reasonable approximation for the as-deposited melt pool formed during PBF-LB builds. Different alloy combinations were laser glazed with a fixed process parameter set, resulting in melt pools with different sizes, microstructures, and hardness. The obtained microstructural features in these melt pools provided information on effectiveness of B for grain refinement in the PBF-LB process. This research helps to better understand the microstructural evolution of Ti-6Al-4 V and related alloys under rapid solidification conditions, offering, in turn, insights for improving alloys for use in additive manufacturing. In addition, the potential to manipulate grain structure through strategic alloying additions (such as those presented in this study) could enhance printed material properties, including strength and fatigue resistance. Therefore, the findings in this study contribute not only to the understanding of microstructural evolution in PBF-LB processes but also pave the way for the development of PBF-LB material with superior properties.

2. Materials and methods

2.1. Manufacturing of specimens: arc melting and laser glazing

Ti-6Al-4 V-xB alloy buttons were prepared by melting amorphous B powder (with 99.5% purity and an average particle size range of 70 nm (supplier: Nanoshell)) and fragments of Ti-6Al-4 V Gd23. A total of thirteen different Ti-6Al-4 V-xB compositions ranging from 0 wt% to 2.5 wt% were melted in a protective argon atmosphere using arc melting (MAM1 Beuhler, Bodelshausen, Germany). The arc was first used to melt a titanium getter, which is designed to react with the gas species present in the melting chamber, and then each alloy composition, each approximately 3 g, were heated and held in a well-stirred molten state for a few seconds to form a homogenous mixture. The melting and flipping of the formed buttons were repeated four times to connectively mix and uniformly distribute the alloying additions throughout the button.

Laser glazing, which is a surface-melting technique in which a high-

energy laser beam traverses the surface of a metal part, creating a thin layer of melted material followed by rapid solidification, was performed on such Ti-6Al-4 V-xB alloy buttons in a commercially available Renishaw AM400 machine. This commercial system is equipped with a maximum laser power of 400 W and employs a 70 μ m spot diameter ytterbium fibre laser with a wavelength of 1064 nm. The laser is power modulated to achieve pulsed output and focuses at one point for a set period (ET, exposure time) at a defined power (P), then immediately moved to the next point, and the exposure process was repeated. The distance between the adjacent points is defined as the point distance (PD). To limit the oxidation, the chamber was filled with argon gas to maintain the oxygen content below 100 ppm. The flat surface of the buttons was melted line-by-line using parameters listed in Table 1 to replicate the deposition of a single-layer in PBF-LB, albeit without powder. The applied process parameter set here is the standard process parameters to PBF-LB print Ti-6Al-4 V in the Renishaw AM400 system.

2.2. Microstructural characterisation

The laser glazed titanium alloy samples were sectioned to expose the transverse cross-sections of the tracks formed by the laser. The cross-sectional samples were mounted in conductive epoxy resin and prepared using standard metallographic procedures. The microstructural analysis was carried out with an optical microscope (Nikon Eclipse LV100ND) and field emission scanning electron microscope (JEOL 7100 F FEG-SEM) equipped with Oxford Instruments NordlysMax3 electron backscatter diffraction (EBSD) detector and Oxford Instruments Advanced X-max 150 energy dispersive spectroscope (EDS) detector.

Microstructural characterisation was conducted in the middle region of the cross-sections to avoid boundary effects. Post-processing of EBSD data was performed using AZtecCrystal software and MTEX toolbox in MATLAB. The average grain sizes of the alloy compositions were measured by a line intercept method on post-processed EBSD images and the OM/SEM images taken from the sample surfaces. The melt pool depths were measured using ImageJ software on band contrast images obtained after the EBSD measurement of the samples. The TEM thin lamellae were prepared by focused ion beam (FEI Quanta200 3D DualBeam FIB/SEM). The diffraction patterns and the elemental composition of samples were acquired using a transmission electron microscope (JEM-2100 F FEG-TEM and JEM-2100 + S/TEM). Oxford Instruments 80 mm X-Max system and Gatan Enfinitum EELS detector were used for energy dispersive x-ray spectroscopy (EDS) and electron energy loss spectroscopy (EELS) during TEM analysis.

Microhardness testing was carried out using a Wilson VH3100 tester. A load of 500 g with dwell time of 10 s was used for indentation. The hardness was measured at 30 different locations that were uniformly distributed across the laser glazed surface, and average hardness value of the melt pools was calculated along with standard error. Phase identification prior and after the laser glazing of alloy buttons was carried out with X-Ray Diffraction (XRD) in a Bruker D8 Advance with DaVinci device in Bragg-Brentano configuration with Cu K α radiation at an energy of 40 kV and 40 mA, using continuous scan mode over a wide range of $2\theta = 20^\circ - 95^\circ$ with a step size of 0.01° and a dwell time of 5 s. The full width at half-maximum (FWHM) and peak fits were obtained using the pseudo-Voigt function in the commercially available Diffrac. Eva software.

Table 1
Process parameters used for single-layer pad laser glazing of the Ti-6Al-4 V-xB alloy buttons.

Surface Glazing Parameters	Values
Laser Power (W)	200
Point Distance (μ m)	75
Exposure Time (μ s)	50
Hatch Distance (μ m)	65

3. Results

3.1. Hardness and melt pool variation of Ti-6Al-4 V-xB alloys

Fig. 1(a) shows the average microhardness values of laser surface glazed regions of Ti-6Al-4 V-xB alloy composition. The average microhardness of laser surface glazed Ti-6Al-4 V-xB alloy compositions were found to increase linearly with the addition of B from approx 356HV (base alloy) to approx 492HV for 2.5 wt% B alloy (approx. 12% increase). This increase can be attributed to the formation of dispersed hard nano sized TiB whiskers in the Ti-6Al-4 V matrix. The pinning effect of nano TiB may lead to the formation of very fine grains, which is an additional contributing factor to the observed increase in hardness. B addition is not only influencing average micro hardness value of the alloy compositions but also affecting melt pool depth. The variation of melt pool depths as a function of B concentration can be seen in Fig. 1 (b). As in the average hardness values, the melt pool depth has dramatically increased with the addition of 0.1 wt% B. There is a good linear correlation between the measured melt pool depth and B concentration in Ti-6Al-4 V-xB alloys. Upon cooling and at B content exceeding the maximum solubility limit in the α phase, the TiB phase is formed by exothermic reaction. The formation of TiB is accompanied by an energy release of 2.99 kJ/g [41], it is therefore thought that this exothermic reaction might lead to the increase in the life of the melt pool and in turn, the depth and width of the observed track cross-sections.

3.2. Phases identification and analysis of Ti-6Al-4 V-xB alloys

The XRD patterns in Fig. 2 show the phases present in surface laser glazed Ti-6Al-4 V-xB alloy buttons. The dominant phase present is α -titanium or α' martensite. Some TiB peaks are overlapping with martensite α' -titanium, making them difficult to discern in the pattern. It should also be noted here that B addition leads to a measurable peak broadening in the spectra such that the full width at half maximum (FWHM) values measured at high angle peaks were increased from 0.597 for base alloy to 1.178 for Ti-6Al-4 V-2.5B alloy. The change in the half-peak width can be interpreted using the Scherrer equation [42]:

$$\beta_s(2\theta)_{hkl} = \frac{K\lambda}{T\cos\theta_{hkl}} \quad (1)$$

where β_s is the grain size contribution to the peak width at half maximum, K is a constant, λ is X-ray wavelength, θ is the diffraction angle, and T is the average thickness of the grains perpendicular to the diffraction plane (hkl). In the XRD analysis of Ti-6Al-4 V-xB alloy buttons, a direct correlation was observed between increasing B concentrations and a decrease in crystallite size, as indicated by the increased half-peak width in the XRD patterns. This empirical observation

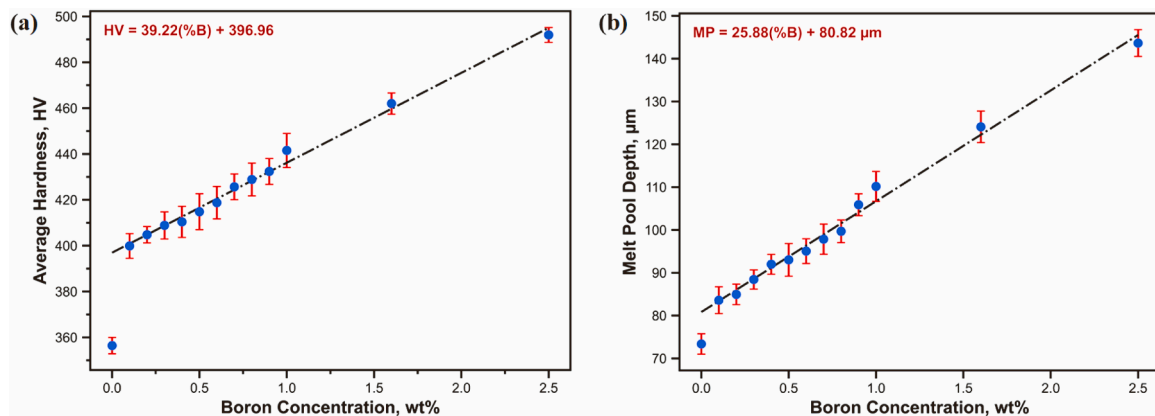


Fig. 1. The variation in (a) average hardness values and (b) melt pool depth as a function of B concentration in laser surface glazed Ti-6Al-4 V-xB alloys prepared by arc melting. Best fit linear expressions, shown in the dotted line, are also added to the figure insets.

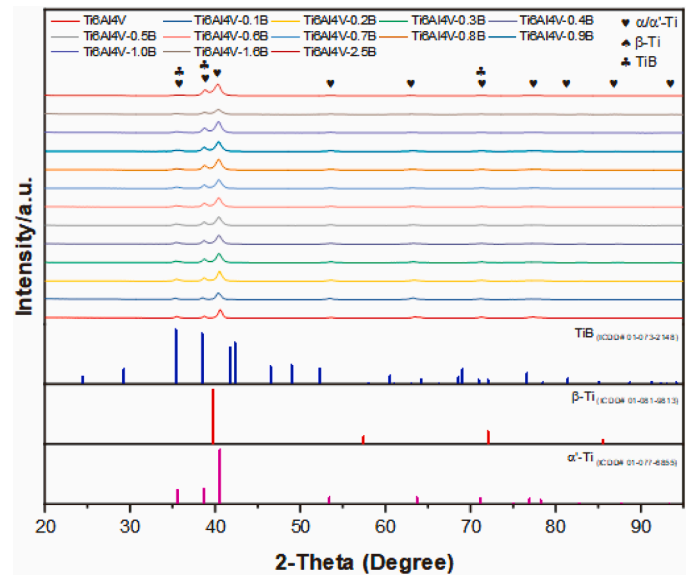


Fig. 2. X-ray diffraction spectrum showing the consisting phases of surface laser glazed Ti-6Al-4 V-xB alloys prepared by arc melting.

suggests a systematic reduction in crystallite size as the B concentration in the alloys increases. Furthermore, it was observed that samples with higher B concentrations exhibited more pronounced peak broadening. The observed broadening was indicative of lattice distortion within the alloy matrix, correlating with the higher concentrations of TiB structures. It should also be noted that there is a hump formation in the XRD peaks around $2\theta = 39^\circ$, which may indicate the presence of β -titanium phase in the microstructure.

Fig. 3 gives the 2θ peak position of the strongest α' -titanium phase as a function of B concentration. It can be noticed that the most intense α' -titanium peak shifts to the left, which implies a decrease in the 2θ angle. The decrease in the martensitic transformation temperature as a function of B concentration provides the opportunity for β to α -titanium transformation [43-45]. The presence of α/α' phase mixture in the surface laser glazed samples could therefore lead to a shifting of 2θ peaks to lower angles.

3.3. Microstructural characterisation of laser glazed Ti-6Al-4 V-xB alloys

Fig. 4 reveals the evolution of microstructural morphologies of surface laser glazed Ti-6Al-4 V-xB alloy buttons. The microstructure of Ti-6Al-4 V alloy is dominated by acicular α' -Ti martensite (Fig. 4(a)). As shown in Fig. 4(b), trace amounts of B addition (0.1 wt%) did not cause

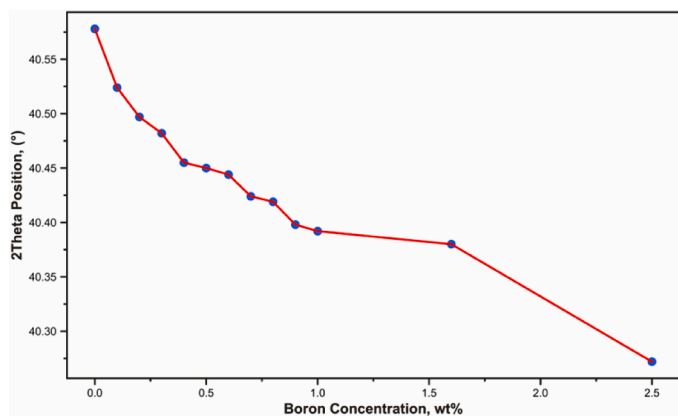


Fig. 3. 2θ peak position of the strongest α' -titanium phase as a function of B concentration.

a significant alteration in the microstructure such that acicular α' martensite is still visible. Nevertheless, trace B addition reduced the width and the length of martensitic α' laths in this alloy. Fig. 4(c) shows that when the B content increased to 0.2 wt%, a second phase starts to appear in the microstructure and shows a fuzzy discontinuous structure alongside acicular α' martensite. This discontinuous structure assumes a quasi-continuous distribution in the microstructure with the increase in the B concentration as seen in Fig. 4(e) – (f). When the B concentration reached about 0.6 wt% B, a full-continuous distribution of the second phase is observed, as seen from Fig. 4(g) – (m). In addition to the network structure present in the alloy compositions, Fig. 4(d) shows that α' is no longer discernible in alloys modified by 0.3 wt% B or more, where $\alpha + \beta$ microstructures appear to be fully developed.

TEM analysis was then used to characterise the microstructural features of the base alloy and the nature of the inter-lath bright phase appearing in Fig. 3(c) – (m). Fig. 5(a) shows the secondary electron image (SE) of the Ti-6Al-4 V alloy composition. The rectangle shows the region of interest where the TEM foil was lifted out. Fig. 5(b) reveals that martensitic α' -titanium is the dominant phase in the specimen. As seen in Fig. 5(c)– (d), the dominant α' martensite in the microstructure is around 200 nm thick and shows high dislocation density. Fig. 5(e) – (h) shows selected area electron diffraction (SAED) patterns taken from within the titanium matrix (e) and within the individual α' -titanium lath (g). SAED patterns obtained from within the titanium matrix confirm that no other phases, such as β -titanium, are observed in the structure, while patterns recorded from within the individual lath confirm that these have an HCP structure and thus shows the martensitic α' nature.

Fig. 6(a) shows the backscatter electron (BSE) image of the Ti-6Al-4 V-1.0B alloy composition, from which the TEM foil was prepared. The TEM bright-field micrograph in Fig. 6(b) reveals that α' martensitic is the dominant phase in the specimen. Additionally, TiB structures are well visible, decorating α' grain boundaries. As seen in Fig. 6(c)– (d), the dominant α' martensite in the microstructure is formed as a fine needle-like α' martensite, indicating that the growth of α' martensite is restrained by the presence of in-situ formed TiB structures. The crystallographic structure of TiB in titanium matrix composites, commonly known as the B27 structure, has been previously reported by Lu et al. [46,47]. The TiB with the B27 structure exhibited a pronounced preferential growth along the [010] direction, resulting in a needle-like morphology characterised by a hexagonal cross-section [32,48,49]. Fig. 6(b) and (e) show the bright-field images of TiB structures formed in a cellular-type structure, indicating that fully nanoscale TiB structures were in-situ formed in the titanium matrix after laser surface glazing. Fig. 6(f) illustrates high-resolution TEM (HRTEM) images of TiB structures as well as its corresponding fast Fourier transform (FFT) profile in region A (Fig. 6(g)), revealing only the B27 structure of TiB. Therefore, the TiB structures in the present study are assumed to have the stable

B27 orthorhombic structure, growing with needle-like morphology. It is also noted here that a high density of faults was visible within these reinforcements as seen in Fig. 6(i). Furthermore, ascribed to the mismatch of thermal expansion between ceramic reinforcements and the titanium matrix, dislocations are present around TiB structures in the matrix [50–52]. To further investigate the reinforcement-matrix interface of the in-situ synthesised TiB structures, HRTEM was also conducted on the interface between TiB structure and α' -Titanium. A clean interface seen in Fig. 6(h) indicates a good interfacial bonding between TiB and titanium matrix at the atomic scale. Because of titanium's α phase ultra-low solid solubility for B, there is virtually no possibility for B composition gradients to form along the precipitates. The pronounced streaking in the SAED patterns shown in Fig. 6(j) and (k) can be attributed to the lots of stacking faults within the TiB (B27) structure along the (011) direction. It is worth noting that Thon rings, observed in Fig. 6(g), (j) and (k), are a characteristic phenomenon identified in the power spectra of micrographs obtained through bright-field (BF) transmission electron microscopy (TEM) imaging [53]. These rings arise as a result of the contrast transfer function, which modulates the Fourier transform of the object based on defocus variations.

Fig. 7 shows the elemental distribution of the Ti-6Al-4 V-1.0B alloy by TEM electron-dispersive spectroscopy (EDS) and electron energy loss spectrometry (EELS). The EDS elemental mapping results of a selected area of interest indicate a homogeneous distribution of Ti (Fig. 7(c)) and V (Fig. 7(e)) within the matrix, while alloying element Al (Fig. 7(d)) exhibit different partitioning characteristics in the titanium matrix. The EDS mapping confirms a microstructural composition predominantly comprising of martensitic α' titanium and titanium boride (TiB) phases, with an apparent absence of the β -titanium phase. Fig. 7(f) reveals that B forms a quasi-continuous network. A comparison between Fig. 7(e) and Fig. 7(f) implies that B-enriched regions are depleted in Al while preserving a similar Ti content as the matrix. EELS analysis is carried out in the selected area of interest to produce a better signal to noise ratio and higher spatial resolution for light elements, as shown in Fig. 7(h). Fig. 7(i) – (l) shows the EELS spectra for elemental distributions, an FFT image of background subtracted EELS spectra, and the elemental distribution of B and Ti, respectively. The EELS elemental mapping indicates a homogeneous distribution of Ti in the matrix (Fig. 7(k)) and B-enriched regions (Fig. 7(l)), which confirms the results observed in TEM EDS mapping. These elemental maps evidence the presence of in-situ synthesised TiB in the Ti-6Al-4 V-xB alloy compositions, which are shown as the white-contrast phase in SEM secondary electron images of Ti-6Al-4 V-xB alloy compositions.

3.4. Assessment of prior β -grain size of Ti-6Al-4 V-xB alloys

Fig. 8 shows the reconstructed prior β -grains of surface laser glazed Ti-6Al-4 V-xB alloy compositions. The electron backscatter diffraction analysis showed that Ti-6Al-4 V alloy consists of a large columnar prior β -titanium grains. Micrographs of the surface laser glazed alloy compositions with the increasing B concentration show a significant reduction in the grain size. Upon subjecting the base alloy to surface laser glazing, an indiscernible reduction in the average grain size is observed, suggesting that the original grains are epitaxially grown from the prior β -grains. Upon introducing a nominal 0.1 wt% B modification to the alloy, there is a discernible reduction in grain size, indicating a clear impact of B addition on grain refinement. Moreover, with a subsequent increase in B concentration to 0.2 wt%, the grain size is further reduced, suggesting the potential for continued improvement in grain refinement with higher B contents. Increasing the added B concentration up to 2.5 wt% causes a significant grain refinement in the alloy compositions such that the microstructure consists of near-equiaxed and/or equiaxed prior β -grains. It can be from these results, it can be deduced that with the increase of B concentration, the number of in-situ synthesised TiB that can act as heterogenous nucleation sites increases, and so in-situ

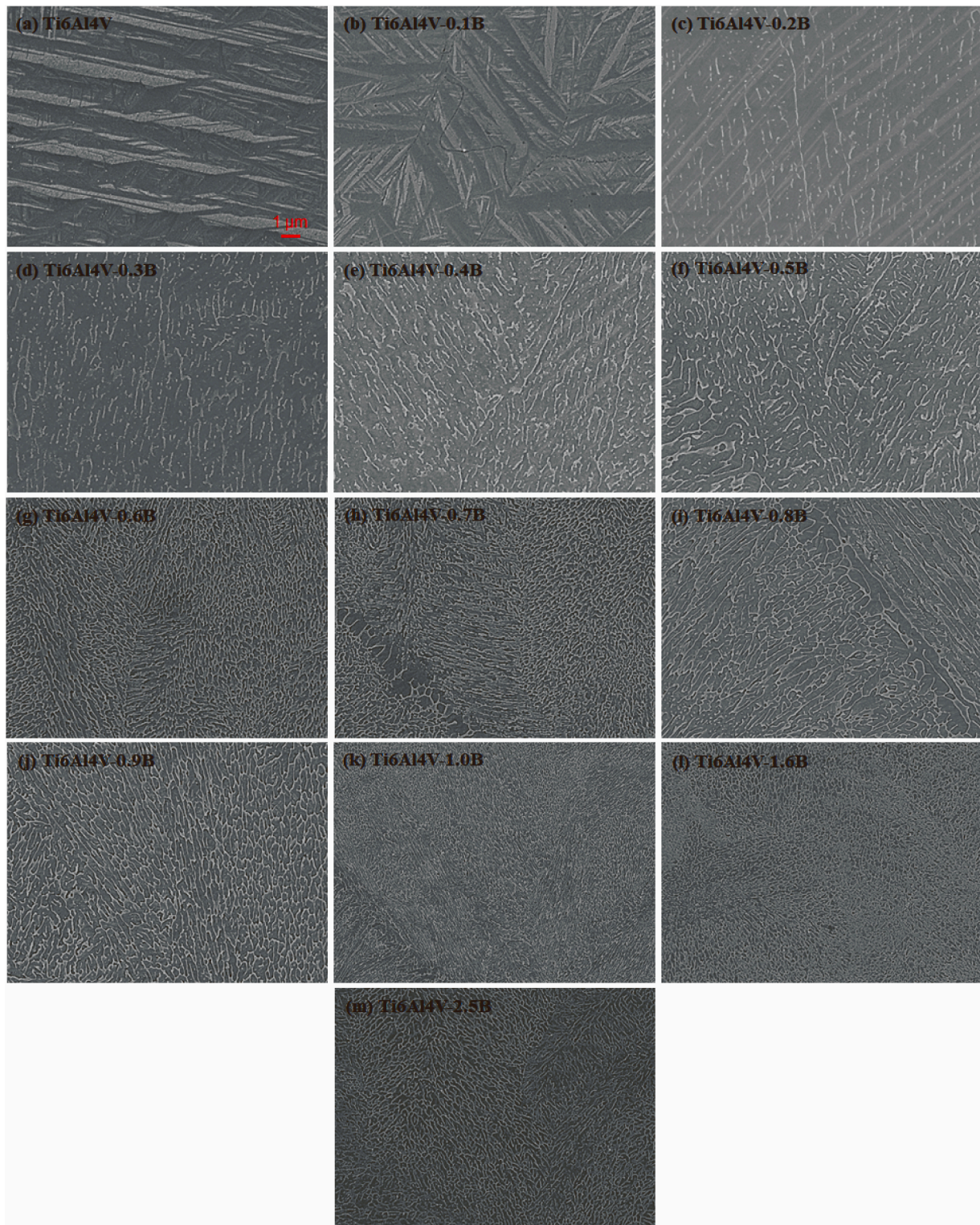


Fig. 4. SEM images (SE mode) showing the microstructural arrangement in laser glazed Ti-6Al-4 V-xB arc melted with 13 different amounts of B.

grain refinement becomes clearly evident as can be seen from Fig. 8.

The average values of length, width and aspect ratio of the α -laths in surface laser glazed Ti-6Al-4 V-xB alloy compositions are given in Fig. 9. With increasing B concentration, the lengths and aspect ratios of α -laths dramatically decrease, while their widths significantly increase. The 0.1 wt% B addition reduces the average length and aspect ratio of the α -laths by about 8% and 13%, respectively, when comparing with the α -laths of Ti-6Al-4 V alloy. When the addition of B increases further, the

average length and aspect ratio of α -laths are reduced more dramatically, when compared with the α -laths of Ti-6Al-4 V alloy. The variation in α -lath size is due to the combined effects of grain refinement and cooling rate.

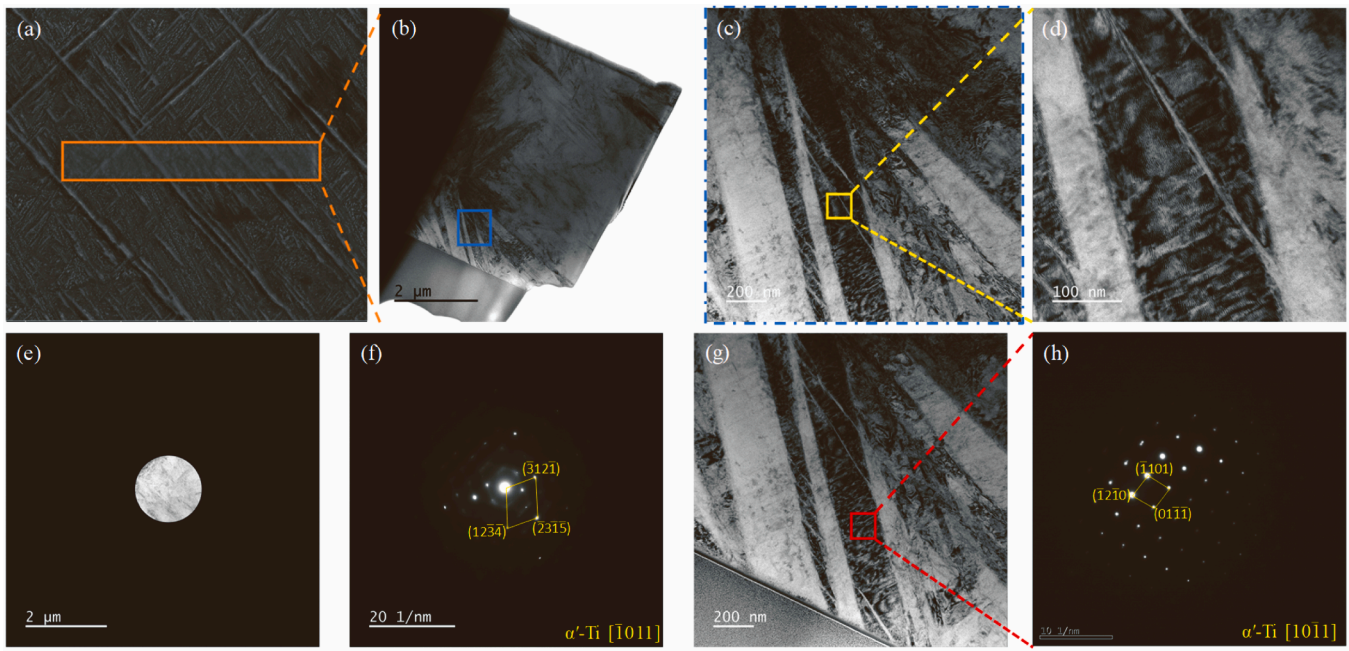


Fig. 5. SEM and TEM micrographs of the laser surface glazed base Ti-6Al-4 V alloy: (a) Secondary electron image of titanium matrix and (b) Bright-field image of the TEM foil showing α' martensite; (c) Bright-field morphology of the α' martensite; (d) Higher magnified brightfield image of a α' -martensite; (e) TEM aperture size showing the region of interest; (f) the corresponding SAED pattern of the region of interest; (g) Bright-field image showing α' -titanium; (h) Corresponding SAED pattern of the region of interest.

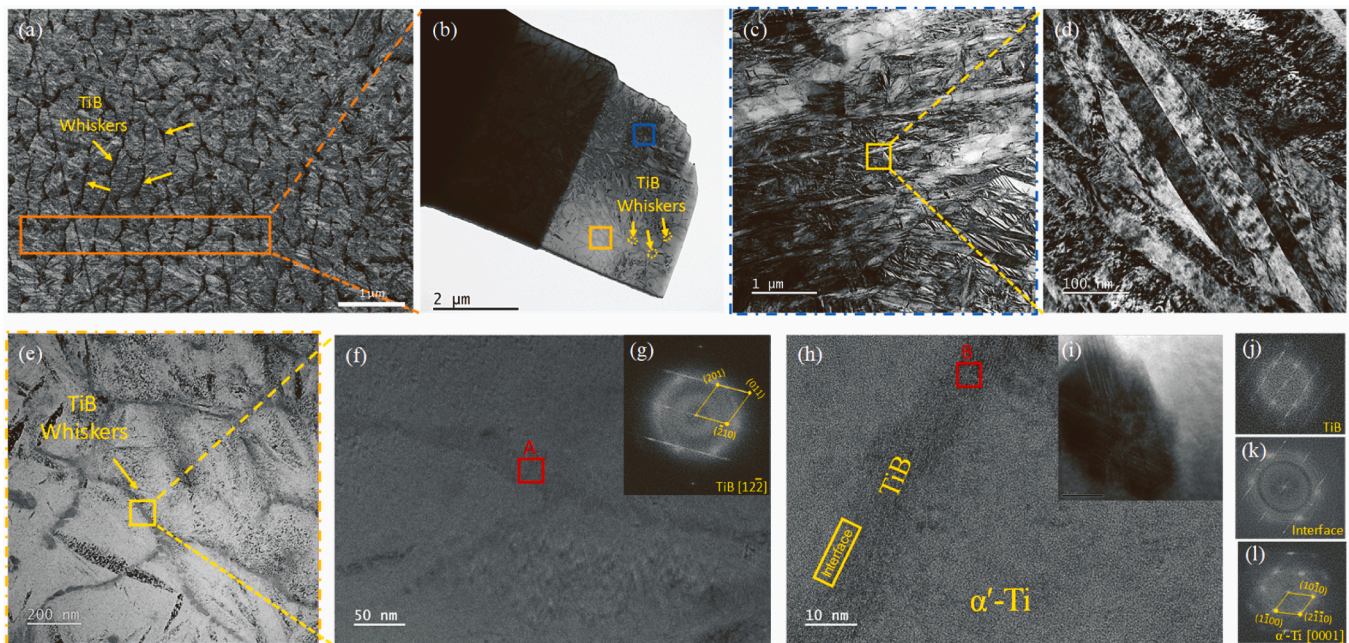


Fig. 6. SEM and TEM micrographs of the laser surface glazed Ti-6Al-4 V-1.0B alloy: (a) Backscattered electron image of TiB structures and titanium matrix and (b) Bright-field image of the TEM foil showing α' martensite and cellular-typed TiB structure; (c) Bright-field morphology of the α' martensite; (d) Higher magnified brightfield image of a α' -martensite; (e) Bright-field morphology of the TiB structure; (f) HRTEM image; (g) the corresponding FFT profile in region A (inset) of TiB structure; (h) HRTEM image of a clean α' -Titanium/TiB interface; (i) Region B (inset) of highly faulted TiB; and the FFT profiles of TiB phase (j), interface (k) and α' -Titanium phase (l).

4. Discussion

4.1. Prior β -grain structure refinement

The results suggest that, without any B addition, the Ti-6Al-4 V initially has a columnar prior β -grain morphology, consistent with the

literature. A gradual transition to a predominantly equiaxed grain morphology can be observed with increasing B additions. It is widely acknowledged that the effectiveness of grain refinement is contingent upon the presence of both powerful heterogeneous nucleant particles and solutes that can provide constitutional supercooling. Constitutional supercooling typically occurs when solutes are more soluble in the liquid

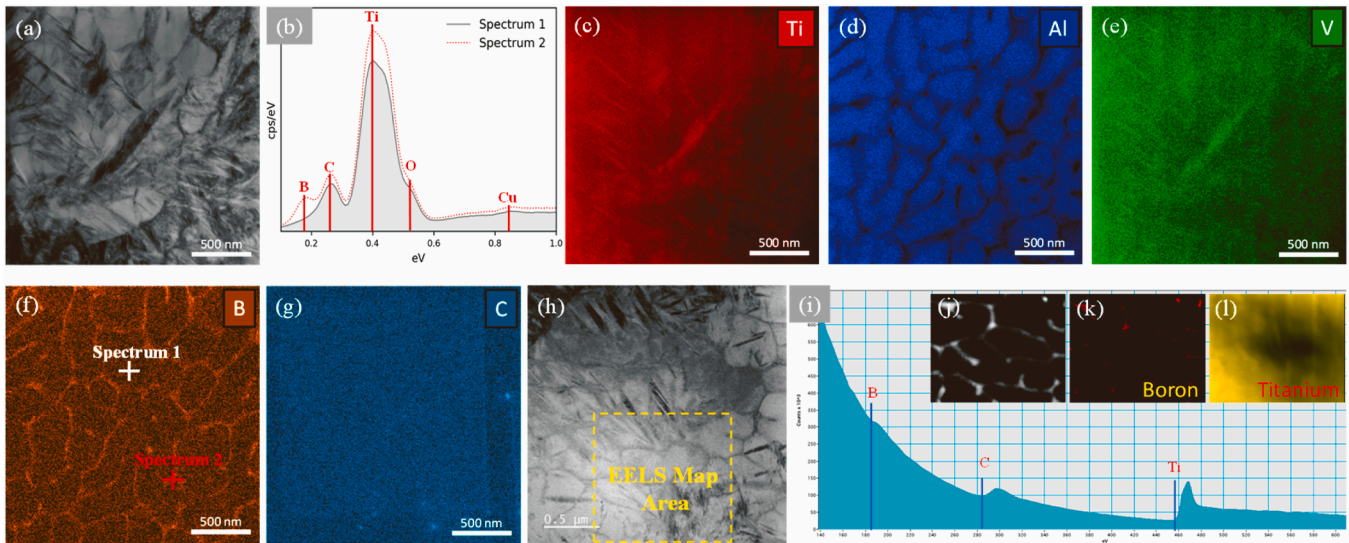


Fig. 7. Elemental distribution in the laser surface glazed Ti-6Al-4 V-1.0B alloy by TEM-EDS and EELS analysis: (a) TEM bright-field image of EDS map of the selected area of interest; (b) EDS spectrum of the selected regions; EDS mapping for the bright-field image showing element distributions of (c) Ti, (d) V, (e) Al, (f) B and (g) C; (h) TEM bright-field image of EELS map of the selected area of interest; (i) EELS mapping for the bright-field image showing (j) integrated signal over the zero-loss peak and B peak and corresponding element distributions of (k) B and (l) Ti.

phase than in the solid phase, causing the liquid ahead of the solid-liquid interface to be cooled below the liquidus point of the alloy.

Fig. 10 schematically presents the columnar and equiaxed grain structure formation of Ti-6Al-4 V-xB in different locations. During surface laser glazing of a TiB reinforced titanium substrate, a melt pool would be created. According to the Ti-6Al-4 V-B pseudo-binary phase diagram [54], the B content in solid and/or liquid phases is not in a thermodynamic equilibrium condition. Therefore, TiB phases will be decomposed into the liquid/melt via diffusion [55]. As the temperature at the bottom of the melt pool reaches the liquidus point, the initial clusters of primary β -Ti grains start to nucleate and growth, while B continues to be rejected into the liquid, leading to the segregation of B ahead of the solidification front. The enrichment of B reduces the liquidus temperature, creating a zone of constitutional supercooling (ΔT_{CS}) [30].

At the early stage of solidification, the melt pool still has a highly steep temperature gradient (G) due to the rapid and intense energy input, resulting in a significant Marangoni effect, as extensively reported in the literature [56]. This effect induces intricate fluid convection patterns within the melt pool and is believed to rearrange the distribution of the solutes [50]. As a consequence, the expelled B is partly transported away from the solid/liquid interface, thereby diminishing the enrichment of solutes locally and limiting the constitutional supercooling (ΔT_{CS}) achieved. Without adequate nucleation ahead of the solidification front, the primary β -Ti grains will grow epitaxially, forming columnar dendritic grains, as shown in Fig. 10 (a).

As the solidification proceeds, the temperature gradient reduces, and the Marangoni convection is greatly weakened, which helps to achieve a higher ΔT_{CS} . Meanwhile, due to the continuous expelling of B into the liquid, an even higher B concentration can be persevered in the remaining melt, as well as in the solid/liquid interface. Therefore, the nucleation behaviour ahead of the solidification front can be significantly promoted to interrupt the original epitaxial growth of the dendrites, as shown in Fig. 10 (b). The competition growth of the newly formed nucleus and the dendritic β -Ti tips leads to the observed in-situ grain refinement in the Ti-6Al-4 V-xB alloy.

It can be noted that, in this study, the obtained grain size continues decreasing with increasing B content. In research conducted by Tamirisakandala et al. [30] on Ti-6Al-4 V castings, it was observed that the addition of B would reach a saturation limit, typically ranging between

0.1 and 0.4 wt%. Beyond this limit, there was no notable additional refinement of the prior β -grains. Once the saturation limit of solutes is reached, it is thought that further refinement can only be achieved by increasing the density of nucleant particles [57].

The current findings indicate that the saturation point in PBF-LB is higher compared to castings, which is expected due to the faster cooling rates experienced in PBF-LB compared to larger castings. The thickness of the B solute diffusion layer ahead of the solid/liquid interface decreases with increasing cooling rate, resulting in a more compressed layer and a maximum ΔT_{CS} closer to the interface [58,59]. As a result, higher levels of solute are necessary to rapidly generate the required ΔT_{CS} .

For the Ti-6Al-4 V-xB alloys, an increase in boron concentration typically leads to a lower cooling rate in the melt pool due to the exothermic reaction of titanium boride (TiB) formation [45,60,61]. Such lower cooling rates, in theory, should result in coarsening of the α/β laths. However, this study observes finer α -laths with increased B concentration. This unexpected refinement in α -lath morphology, even under reduced cooling rates, can be attributed to the enhanced microstructural pinning effects of the TiB structures formed at higher B concentrations. These precipitates act as nucleation sites, exerting a pinning force on migrating grain boundaries during the $\beta \rightarrow \alpha$ phase transformation [20,38]. This pinning restricts the growth of α -laths, overriding the conventional coarsening effect of slower cooling rates. Therefore, the finer α -lath structure in these B-enriched alloys is a direct consequence of the influence of TiB structures. It demonstrates that the microstructural evolution in the Ti-6Al-4 V-xB alloys is more significantly governed by B-induced phase stabilisation and TiB-mediated boundary pinning.

4.2. Formation of TiB network structure

In the context of Ti-6Al-4 V-xB alloys subjected to rapid solidification, TiB intermetallic formed in the studied alloy composition, which aligns with thermodynamic predictions and kinetic behaviour as well as pseudo-binary phase diagram of Ti6Al4V-B system shown elsewhere [54]. Ti_3B_4 phases are theoretically unstable in the employed conditions due to a need of high-purity Ti, a reducing atmosphere, and their limited stability regions [62]. Furthermore, despite the favourable Gibbs free energy for the formation of TiB_2 , the kinetics of boron diffusion and the

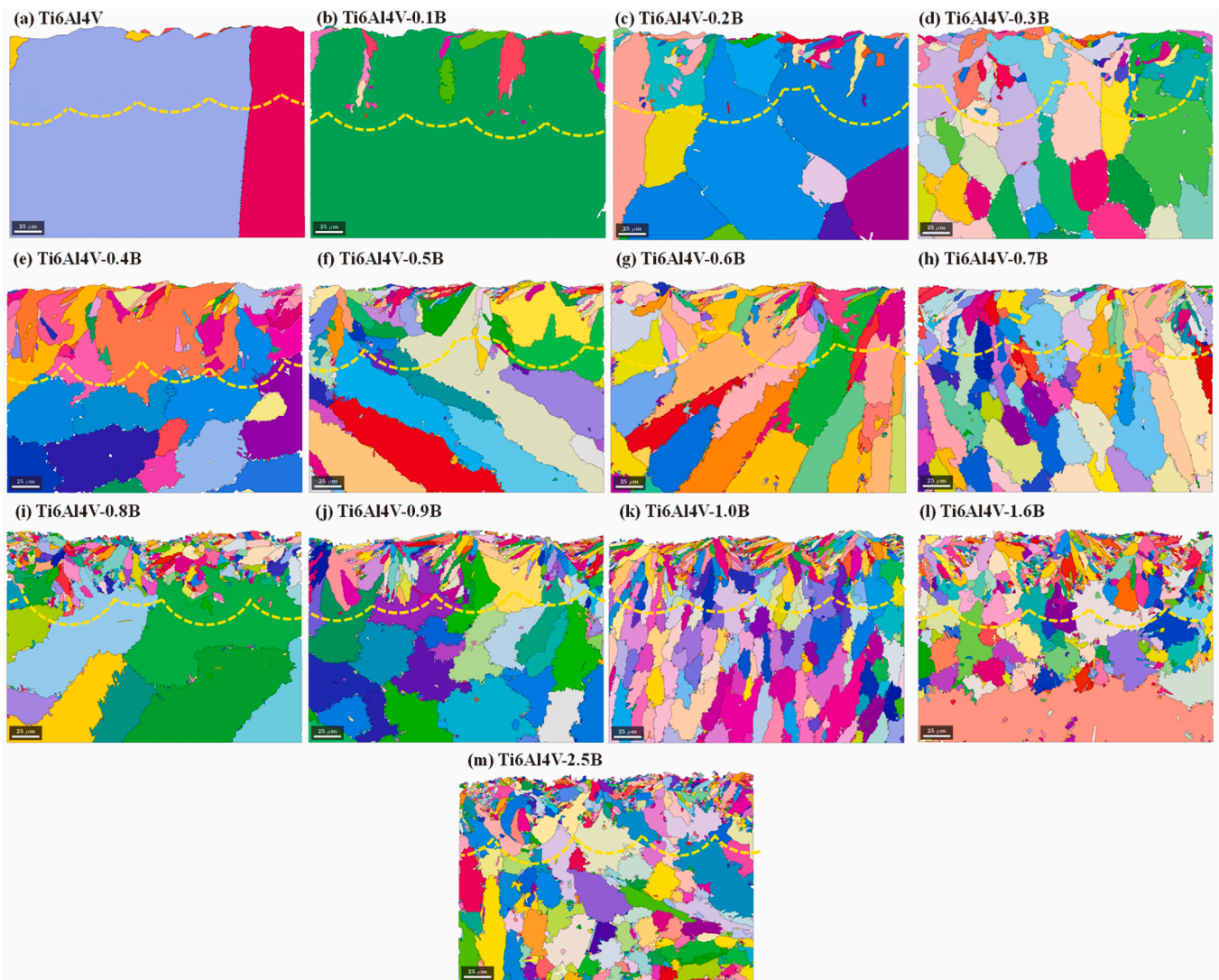


Fig. 8. Reconstructed prior β -grain sizes superimposed on the band contrast image of surface laser glazed Ti-6Al-4 V-xB alloy compositions. Yellow dashed line indicates the melt pools formed after laser glazing.

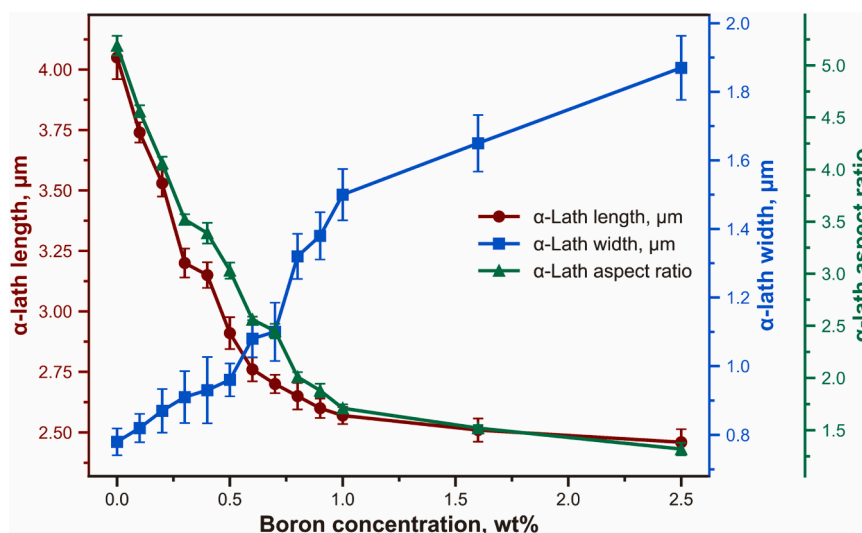


Fig. 9. The effect of B concentration on the measured α -laths sizes of surface laser glazed Ti-6Al-4 V-xB alloy compositions.

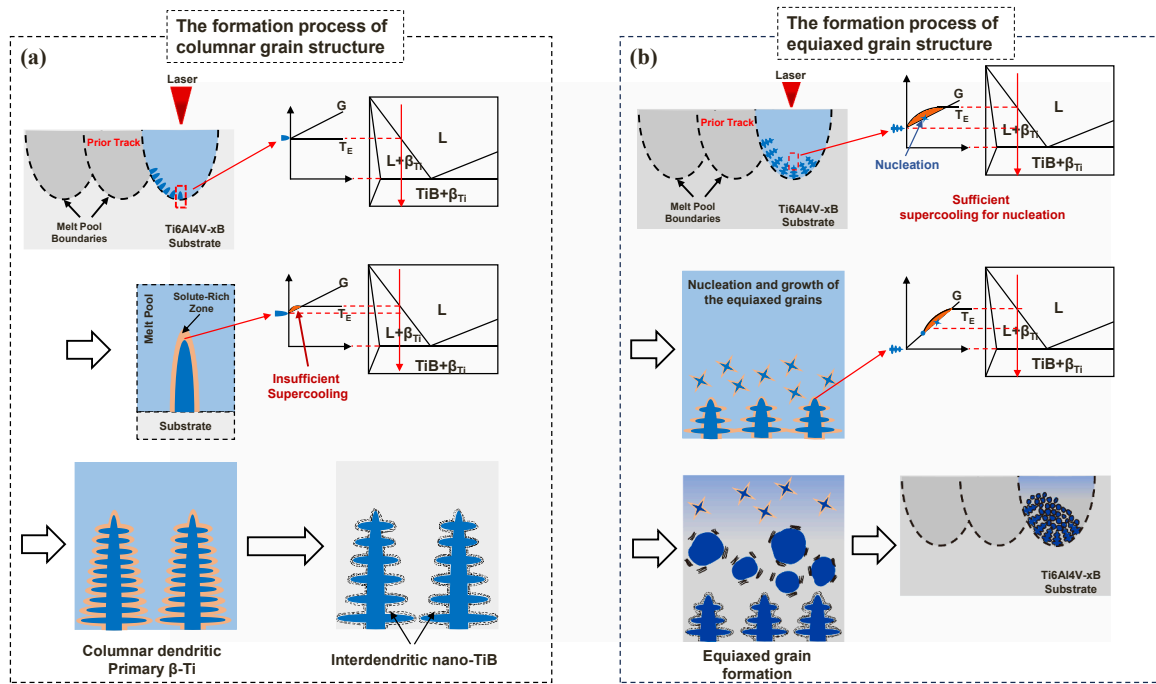


Fig. 10. The schematic of the formation process of (a) columnar grain structure and (b) equiaxed grain structure in the Ti-6Al-4 V-xB alloy compositions.

rapid growth rate of TiB dominate, causing TiB₂ to readily convert to TiB through a reaction between TiB₂ and liquid metal, which has a more favourable energy profile. The rapid cooling rates inherent to PBF-LB processes typically promote the formation of metastable phases; however, in this scenario, they instead contribute to the kinetic drivers that favour TiB formation. Consequently, the solidification path is effectively steered towards TiB, precluding the stabilisation of TiB₂ or Ti₃B₄ phases. As an intermetallic phase, its presence would considerably affect the mechanical properties of the materials. Understanding the formation and distribution of TiB in Ti-6Al-4 V-xB alloy composition during solidification relies on the solute distribution (Al, V, and B) at the solid-liquid interface.

The accumulation of B on the liquid side of the interface, caused by the addition of B and increased supercooling, intensifies the segregation of Al and V [63]. The varying B concentrations within the melt pool

would lead to diverse fluid convections, resulting in distinct microstructures. In the case of relative low B concentrations, TiB is primarily distributed along grain boundaries, as observed in Fig. 4(c), which can be attributed to the less turbulent behaviour of the melt pool under these conditions, leading to uneven boron enrichment, as illustrated in Fig. 11 (a) and (b). In the melt pool with low B concentration, the initial solidification commences at the melt pool boundaries, rejecting B into the remaining melt, resulting in increased B concentration in the liquid. In areas where the boron content exceeds the eutectic composition, there is a tendency for TiB to precipitate preferentially during solidification (Fig. 11 (c)), followed by subsequent precipitation of the β-titanium phase (Fig. 11 (d)). With the ongoing growth of the β grains, TiB is displaced to the grain boundaries (Fig. 11 (e)), resulting in its accumulation and distribution along these boundaries (Fig. 11 (f)). The changes in boron concentration within the melt pools thus influence the

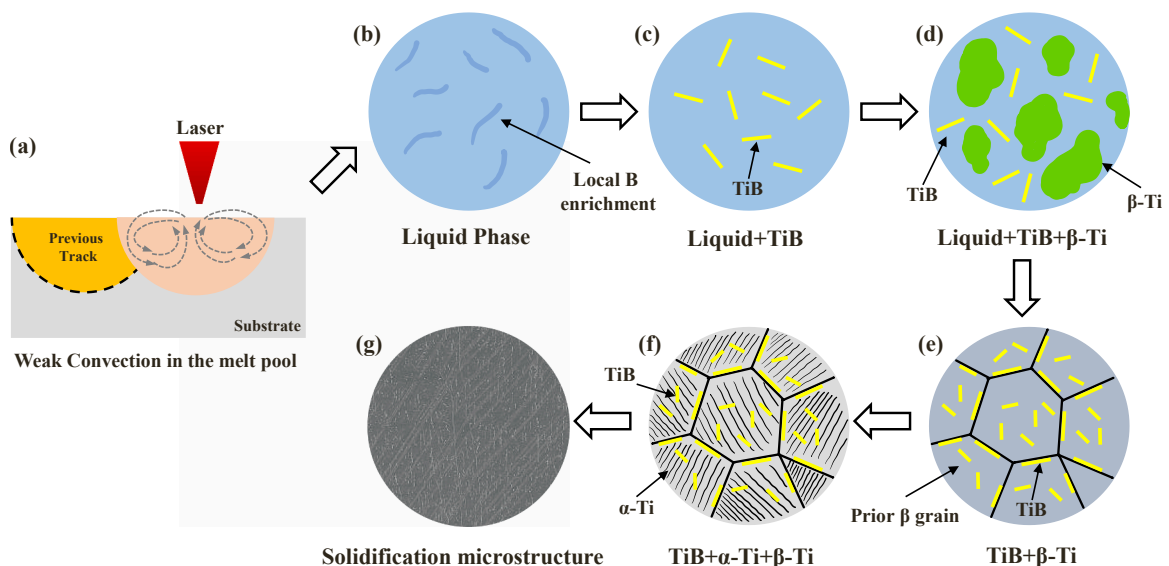


Fig. 11. The schematic solidification process diagram of low-B concentration containing Ti-6Al-4 V-xB alloy during surface laser glazing.

fluid dynamics during the solidification process, leading to a redistribution of TiB within the previously formed β -grains (Fig. 11 (g)).

In the case of higher B concentrations, the B-modified Ti-6Al-4 V alloy demonstrates uniform distribution of B under both macroscopic and microscopic conditions (Fig. 12 (b)). This uniformity results from the intense convection within the melt pool, illustrated in Fig. 12 (a). This relates to solidification taking place within the hypoeutectic range. During solidification, the prior β -titanium phase first nucleated and grew in the liquid phase (Fig. 12 (c)). The non-equilibrium rapid solidification in the melt pool, accompanied by constitutional undercooling, will result in solute partitioning. This process facilitates the growth of β -Ti and the segregation of boron, leading to the development of cellular morphology, as illustrated in Fig. 12 (d). When the solidification temperature decreases to the eutectic temperature, the eutectic (β -Ti + TiB) begins to grow in the remaining liquid phase. Because of the narrow solidification temperature range, both the content of the eutectic components and the TiB size are suppressed (Fig. 12 (e)). As the solidification progresses and the temperature falls below the β to α phase transition temperature, the β -Ti phase transforms into the α phase, as shown in Fig. 12 (f). In regions with a high boron concentration, TiB structures will form a quasi-continuous network microstructure, as evident in the room temperature microstructure shown in Fig. 12 (g). Moreover, the needle-like or whisker-like B27 structure of TiB, with its significant specific surface area, causes TiB whiskers to align and aggregate during formation [46,47], particularly in areas of higher boron content, resulting in the formation of a quasi-continuous network structure.

In this study, the consistent laser surface melting parameters applied to all arc melted buttons aimed to minimize the effects of varying thermal histories, an approach that approximates the thermal behaviour experienced in PBF-LB. While both PBF-LB and laser surface melting involve high-temperature melting and rapid solidification, they differ significantly in their impact on the microstructure of materials. Laser surface melting involves essentially a “single layer” application of a high-energy laser to the surface of a material. This technique is primarily focused on modifying the surface characteristics, where the thermal influence of the laser induces singular melting and rapid solidification event. Each melt pool is partially melted by the neighbouring tracks in the same layer and the high temperature experienced might also induce some solid phase transformation. Similarly, the evolution of the microstructure in PBF-LB results from multiple significant thermal cycles not just from adjacent tracks of the same layer but also from each new deposited layer. In a related publication for example, the authors

demonstrate that during PBF-LB each volume of Ti-6Al-4 V undergoes four to six solid phase transformations using standard processing parameters comparable to those used in the present study [64]. Therefore, the likelihood of martensitic microstructures to decompose during PBF-LP, as discussed in a number of papers such as [3,9,15,65], is significantly higher than in our proposed laser glazing experiments.

5. Conclusion

In this study, a comprehensive investigation of the influence of different B additions ranging from 0.1 wt% to 2.5 wt% on the microstructures of Ti-6Al-4 V alloy was carried out. This work employed a powder-free laser glazing methodology on the flat surface of arc-melted buttons to imitate thermal history under rapid solidification conditions analogous to those encountered in PBF-LB process of different B modified Ti-6Al-4 V alloy. The following conclusions can be drawn from this study:

1. The average hardness values of the surface laser glazed regions increased with the addition of B. This was mainly because of smaller grains and the volume fraction of TiB particles present in the laser glazed areas.
2. The melt pool depth is a function of the B concentration added to Ti-6Al-4 V alloy. The average melt pool depth increased with addition of B. This can be mainly attributed to the in-situ formation of TiB particles within the melt pool and the associated exothermic reaction.
3. Laser surface melting was carried out to simulate thermal history encountered under rapid solidification during the PBF-LB process. The refining of the α -Ti is mainly attributed to the presence of TiB in the prior β -Ti grains, while the refinement of β -Ti phase was caused by the combined effect of B restricting the growth of β -titanium and TiB particles present in the melt pool, acting as a heterogenous nucleation point for β -titanium.
4. The microstructural characterization conclusively demonstrates that across all examined samples with different B concentrations, the microstructure of the laser glazed regions is uniformly characterized by the presence of martensitic α' titanium and titanium boride (TiB) phases, while distinctly lacking the β -titanium phase.
5. The addition of B in laser surface melted Ti-6Al-4 V-xB alloys predominantly forms TiB intermetallic, with no TiB₂ and Ti₃B₄ phases been observed.

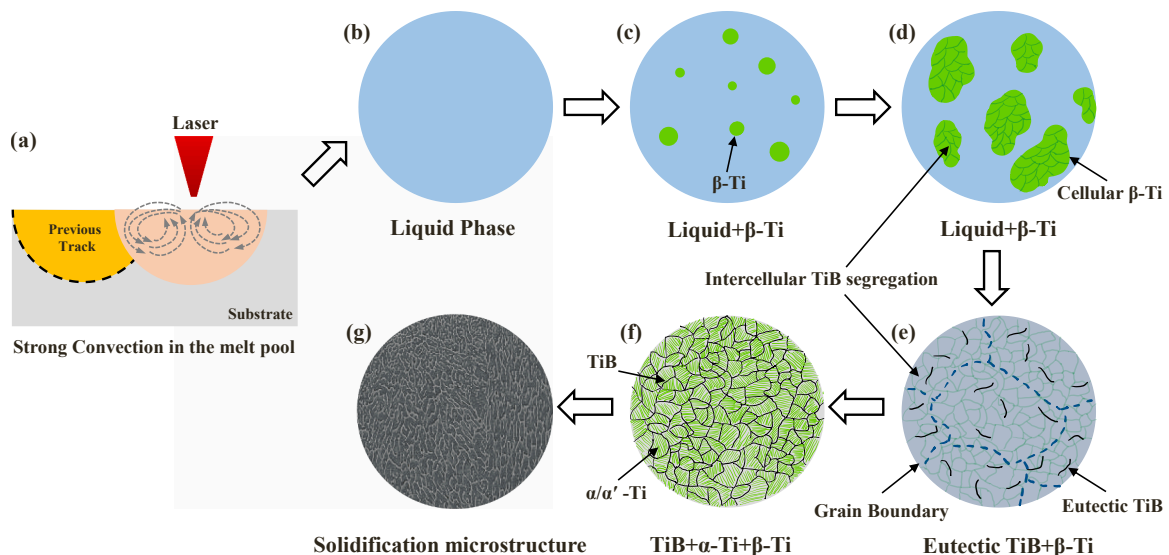


Fig. 12. The schematic solidification process diagram of high-B concentration containing Ti-6Al-4 V-xB alloy during surface laser glazing.

- The results from this study clearly demonstrate that boron concentration of 0.2 wt% or higher can effectively refine the microstructure of the Ti-6Al-4 V alloy. Increasing the boron content beyond this threshold leads to the formation of a quasi-continuous TiB network within the structure, suggesting a critical role of higher boron concentrations in enhancing the alloy's microstructural properties under rapid solidification conditions.
- For the first time, it is presented in this research that the reconstructed β -grains from EBSD are used to assess the extent of refinement achievable with different amount of B addition to Ti-6Al-4 V, particularly at higher hypoeutectic concentrations which has not been previously explored.

CRedit authorship contribution statement

MURRAY James: Writing – review & editing, Supervision, Formal analysis, Conceptualization. **ZOU Zhiyi:** Writing – review & editing, Formal analysis. **HIZLI Huseyin:** Writing – original draft, Methodology, Investigation, Formal analysis, Conceptualization. **Simonelli Marco:** Writing – review & editing, Supervision, Resources, Formal analysis, Conceptualization. **CLARE Adam:** Writing – review & editing, Supervision, Formal analysis, Conceptualization.

Declaration of Competing Interest

The authors declare that they have no known competing financial interests or personal relationships that could have appeared to influence the work reported in this paper.

Data availability

Data will be made available on request.

Acknowledgments

The authors would like to thank Mr. Mark East and Mr. Mark Hardy for their assistance in the laboratory work at the Centre for Additive Manufacturing. Huseyin Hizli thanks Dr Nigel Neate from nano- and micro-research centre (nmRC) in the University of Nottingham for training and access of SEM (EDS), EBSD and TEM. Huseyin Hizli also thanks Dr Stuart Robertson from Loughborough Materials Characterisation Centre for access of TEM.

References

- C. Körner, Additive manufacturing of metallic components by selective electron beam melting—a review, *Int. Mater. Rev.* 61 (5) (2016) 361–377.
- S.L. Sing, J. An, W.Y. Yeong, F.E. Wiria, Laser and electron-beam powder-bed additive manufacturing of metallic implants: a review on processes, materials and designs, *J. Orthop. Res.* 34 (3) (2016) 369–385.
- P. Barriobero-Vila, J. Gussone, J. Haubrich, S. Sandlöbes, J.C. da Silva, P. Cloetens, N. Schell, G. Requena, Inducing stable $\alpha + \beta$ microstructures during selective laser melting of Ti-6Al-4V using intensified intrinsic heat treatments, *Materials* 10 (3) (2017), <https://doi.org/10.3390/MA10030268>.
- J. Haubrich, J. Gussone, P. Barriobero-Vila, P. Kürnsteiner, E.A. Jäggle, D. Raabe, G. Requena, The role of lattice defects, element partitioning and intrinsic heat effects on the microstructure in selective laser melted Ti-6Al-4V, *Acta Mater.* 167 (2019) 136–148.
- S. Cao, Z. Chen, C.V.S. Lim, K. Yang, Q. Jia, T. Jarvis, D. Tomus, X. Wu, Defect, microstructure, and mechanical property of Ti-6Al4V alloy fabricated by high-power selective laser melting, *JOM* 69 (12) (2017) 2684–2692.
- J. Yang, H. Yu, J. Yin, M. Gao, Z. Wang, X. Zeng, Formation and control of martensite in Ti-6Al-4V alloy produced by selective laser melting, *Mater. Des.* 108 (2016) 308–318.
- M. Muhammad, J.W. Pegues, N. Shamsaei, M. Haghshenas, Effect of heat treatments on microstructure/small-scale properties of additive manufactured Ti-6Al-4V, *Int. J. Adv. Manuf. Technol.* 1–12 (2019), <https://doi.org/10.1007/s00170-019-03789-w>.
- J. Yang, H. Yu, Z. Wang, X. Zeng, Effect of crystallographic orientation on mechanical anisotropy of selective laser melted Ti-6Al-4V alloy, *Mater. Charact.* 127 (2017) 137–145.
- W. Xu, M. Brandt, S. Sun, J. Elambasseril, Q. Liu, K. Latham, M. Qian, Additive manufacturing of strong and ductile Ti-6Al-4V by selective laser melting via in situ martensite decomposition, *Acta Mater.* 85 (2015) 74–84.
- B. He, W. Wu, L. Zhang, L. Lu, Q. Yang, Q. Long, K. Chang, Microstructural characteristic and mechanical property of Ti-6Al-4V alloy fabricated by selective laser melting, *Vacuum* 150 (2018) 79–83.
- P. Magnus Neikter, R. Åkerfeldt, Pederson and Marta-Lena Antti. Microstructure characterisation of Ti-6Al-4V from different additive manufacturing processes. IOP Conference Series: Materials Science and Engineering, IOP Publishing, 2017.
- P. Mercelis, J.P. Kruth, Residual stresses in selective laser sintering and selective laser melting, *Rapid Prototyp. J.* (2006).
- M. Neikter, R. Woracek, T. Maimaitiyili, C. Scheffzük, M. Strobl, M.L. Antti, P. Rollett, Alpha texture variations in additive manufactured Ti-6Al-4V investigated with neutron diffraction, *Addit. Manuf.* 23 (2018) 225–234.
- L. Qian, J. Mei, J. Liang, X. Wu, Influence of position and laser power on thermal history and microstructure of direct laser fabricated Ti-6Al-4V samples, *Mater. Sci. Technol.* 21 (5) (2005) 597–605.
- A. Zafari, M.R. Barati, K. Xia, Controlling martensite decomposition during selective laser melting to achieve best ductility in high strength Ti-6Al-4V, *Mater. Sci. Eng.: A* 744 (2019) 445–455.
- S.A. Oh, R.E. Lim, J.W. Aroh, A.C. Chuang, B.J. Gould, B. Amin-Ahmadi, A. C. Bjerlén, High speed synchrotron X-ray diffraction experiments resolve microstructure and phase transformation in laser processed Ti-6Al-4V, *Mater. Res. Lett.* 9 (10) (2021) 429–436.
- T. Vilaro, C. Colin, J.D. Bartout, As-fabricated and heat-treated microstructures of the Ti-6Al-4V alloy processed by selective laser melting, *Metal. Mater. Trans. A* 42 (2011) 3190–3199.
- C. De Formanoir, S. Michotte, O. Rigo, L. Germain, S. Godet, Electron beam melted Ti-6Al-4V: microstructure, texture and mechanical behavior of the as-built and heat-treated material, *Mater. Sci. Eng. A* 652 (2016) 105–119.
- V. Popov, et al., Effect of hot isostatic pressure treatment on the electron-beam melted Ti-6Al-4V specimens, *Procedia Manuf.* 21 (2018) 125–132.
- A. Xue, X. Lin, L. Wang, J. Wang, W. Huang, Influence of trace B addition on microstructure, tensile properties and their anisotropy of Ti-6Al-4V fabricated by laser directed energy deposition, *Mater. Des.* 181 (2019) 107943.
- X. Lin, T.M. Yue, H.O. Yang, W.D. Huang, Solidification behavior and the evolution of phase in laser rapid forming of graded Ti-6Al-4V-Rene88DT alloy, *Metall. Mater. Trans. A* 38 (1) (2007) 127–137.
- M.Y. Mendoza, P. Samimi, D.A. Brice, B.W. Martin, M.R. Rolchigo, R. LeSar, P. C. Collins, Microstructures and grain refinement of additive-manufactured Ti-xW alloys, *Metall. Mater. Trans. A* 48 (7) (2017) 3594–3605.
- F. Zhang, M. Yang, A.T. Clare, X. Lin, H. Tan, Y. Chen, Microstructure and mechanical properties of Ti-2Al alloyed with Mo formed in laser additive manufacture, *J. Alloy. Compd.* 727 (2017) 821–831.
- M.J. Bermingham, D.H. StJohn, J. Krynen, S. Tedman-Jones, M.S. Dargusch, Promoting the columnar to equiaxed transition and grain refinement of titanium alloys during additive manufacturing, *Acta Mater.* 168 (2019) 261–274.
- A.M. Vilarde, I. Yadroitsev, I. Yadroitsava, M. Albu, N. Takata, M. Kobashi, A. Du Plessis, Manufacturing and characterization of in-situ alloyed Ti-6Al-4V (ELI)-3 at % Cu by laser powder bed fusion, *Addit. Manuf.* 36 (2020) 101436.
- M. Simonelli, D.G. McCartney, P. Barriobero-Vila, N.T. Aboulkhair, Y.Y. Tse, A. Clare, R. Hague, The influence of iron in minimizing the microstructural anisotropy of Ti-6Al-4V produced by laser powder-bed fusion, *Metall. Mater. Trans. A* 51 (5) (2020) 2444–2459.
- M.J. Bermingham, S.D. McDonald, D.H. StJohn, M.S. Dargusch, Beryllium as a grain refiner in titanium alloys, *J. Alloy. Compd.* 481 (1–2) (2009) L20–L23.
- S. Roy, S. Suwas, S. Tamirisakandala, D.B. Miracle, R. Srinivasan, Development of solidification microstructure in B-modified alloy Ti-6Al-4V-0.1 B, *Acta Mater.* 59 (14) (2011) 5494–5510.
- O.O. Bilous, L.V. Artyukh, A.A. Bondar, T.Y. Velikanova, M.P. Burka, M. P. Brodnikovskiy, S.O. Firstov, Effect of B on the structure and mechanical properties of Ti-6Al and Ti-6Al-4V, *Mater. Sci. Eng.: A* 402 (1–2) (2005) 76–83.
- S. Tamirisakandala, R.B. Bhat, J.S. Tiley, D.B. Miracle, Grain refinement of cast titanium alloys via trace B addition, *Scr. Mater.* 53 (12) (2005) 1421–1426.
- A. Helth, U. Siegel, U. Kühn, T. Gemming, W. Gruner, S. Oswald, J. Eckert, Influence of B and oxygen on the microstructure and mechanical properties of high-strength Ti66Nb13Cu8Ni6.8Al6.2 alloys, *Acta Mater.* 61 (9) (2013) 3324–3334.
- M.J. Bermingham, S.D. McDonald, K. Nogita, D.S. John, M.S. Dargusch, Effects of B on microstructure in cast titanium alloys, *Scr. Mater.* 59 (5) (2008) 538–541.
- J. Zhu, A. Kamiya, T. Yamada, W. Shi, K. Naganuma, Influence of B addition on microstructure and mechanical properties of dental cast titanium alloys, *Mater. Sci. Eng.: A* 339 (1–2) (2003) 53–62.
- H. Attar, M. Bönisch, M. Calin, L.C. Zhang, S. Scudino, J. Eckert, Selective laser melting of in situ titanium-titanium boride composites: processing, microstructure and mechanical properties, *Acta Mater.* 76 (2014) 13–22.
- R.R. Rashid, S. Palanisamy, H. Attar, M. Bermingham, M.S. Dargusch, Metallurgical features of direct laser-deposited Ti-6Al-4V with trace B, *J. Manuf. Process.* 35 (2018) 651–656.
- Z. Mahbooba, H. West, O. Harrysson, A. Wojcieszynski, R. Dehoff, P. Nandwana, T. Horn, Effect of hypoeutectic B additions on the grain size and mechanical properties of Ti-6Al-4V manufactured with powder bed electron beam additive manufacturing, *Jom* 69 (2017) 472–478.
- M.J. Bermingham, S.D. McDonald, M.S. Dargusch, Effect of trace lanthanum hexaboride and B additions on microstructure, tensile properties and anisotropy of

- Ti-6Al-4V produced by additive manufacturing, *Mater. Sci. Eng.: A* 719 (2018) 1–11.
- [38] M.J. Bermingham, D. Kent, H. Zhan, D.H. StJohn, M.S. Dargusch, Controlling the microstructure and properties of wire arc additive manufactured Ti-6Al-4V with trace B additions, *Acta Mater.* 91 (2015) 289–303.
- [39] P.K. Verma, S. Warghane, U. Nichul, P. Kumar, A. Dhole, V. Hiwarkar, Effect of B addition on microstructure, hardness and wear performance of Ti-6Al-4 V alloy manufactured by laser powder bed fusion additive manufacturing, *Mater. Charact.* 172 (2021) 110848.
- [40] S.A. Mantri, T. Alam, D. Choudhuri, C.J. Yannetta, C.V. Mikler, P.C. Collins, R. Banerjee, The effect of B on the grain size and texture in additively manufactured β -Ti alloys, *J. Mater. Sci.* 52 (20) (2017) 12455–12466.
- [41] Y.F. Li, H. Xu, Q.L. Xia, X.L. Liu, First-principles calculation of structural and thermodynamic properties of titanium boride, *J. Cent. South Univ. Technol.* 18 (6) (2011) 1773–1779.
- [42] Scherrer, P. (1916). *Gött. Nachr.*
- [43] Y. Horiuchi, T. Inamura, H.Y. Kim, K. Wakashima, S. Miyazaki, H. Hosoda, Effect of B concentration on martensitic transformation temperatures, stress for inducing martensite and slip stress of Ti-24 mol% Nb-3 mol% Al superelastic alloy, *Mater. Trans.* 48 (3) (2007) 407–413.
- [44] H. Li, Z. Yang, D. Cai, D. Jia, Y. Zhou, Microstructure evolution and mechanical properties of selective laser melted bulk-form titanium matrix nanocomposites with minor B4C additions, *Mater. Des.* 185 (2020) 108245.
- [45] A.S. Patil, V.D. Hiwarkar, P.K. Verma, R.K. Khatirkar, Effect of TiB₂ addition on the microstructure and wear resistance of Ti-6Al-4V alloy fabricated through direct metal laser sintering (DMLS), *J. Alloy. Compd.* 777 (2019) 165–173.
- [46] W. Lu, D. Zhang, X. Zhang, R. Wu, T. Sakata, H. Mori, Microstructural characterization of TiB in in situ synthesized titanium matrix composites prepared by common casting technique, *J. Alloy. Compd.* 327 (1-2) (2001) 240–247.
- [47] W.J. Lu, L. Xiao, K. Geng, J.N. Qin, D. Zhang, Growth mechanism of in situ synthesized TiBw in titanium matrix composites prepared by common casting technique, *Mater. Charact.* 59 (7) (2008) 912–919.
- [48] F. Ma, B. Zheng, P. Liu, W. Li, X. Liu, X. Chen, W. Lu, Modeling of effects of thermomechanical processing on elevated-temperature mechanical properties of in situ (TiB+ TiC)/Ti-1100 composite, *J. Mater. Sci.* 51 (2016) 7502–7511.
- [49] M. Fang, Y. Han, Z. Shi, G. Huang, J. Song, W. Lu, Embedding B into Ti powder for direct laser deposited titanium matrix composite: microstructure evolution and the role of nano-TiB network structure, *Compos. Part B: Eng.* 211 (2021) 108683.
- [50] C. Cai, C. Radoslaw, J. Zhang, Q. Yan, S. Wen, B. Song, Y. Shi, In-situ preparation and formation of TiB/Ti-6Al-4V nanocomposite via laser additive manufacturing: microstructure evolution and tribological behavior, *Powder Technol.* 342 (2019) 73–84.
- [51] C. Liu, K.H. Jin, J. Ye, X. Gao, X. Wei, Z. Zhang, H.X. Peng, Additive manufacturing of (TiB+ TiC)/Ti-6Al-4V composites with tailored network reinforcement architecture, *Compos. Commun.* 40 (2023) 101611.
- [52] D. He, H. Wang, W. Huang, X. Chen, G. Lian, Y. Wang, Microstructure and mechanical properties of LaB₆/Ti-6Al-4V composites fabricated by selective laser melting, *Metals* 13 (2) (2023) 264.
- [53] W. Tichelaar, W.J. Hagen, T.E. Gorelik, L. Xue, J. Mahamid, TEM bright field imaging of thick specimens: nodes in Thon ring patterns, *Ultramicroscopy* 216 (2020) 113023.
- [54] Y. He, C. Montgomery, J. Beuth, B. Webler, Melt pool geometry and microstructure of Ti-6Al-4V with B additions processed by selective laser melting additive manufacturing, *Mater. Des.* 183 (2019) 108126.
- [55] X. Tao, Z. Yao, S. Zhang, Reconstruction and refinement of TiB whiskers in titanium matrix composite after electron beam remelting, *Mater. Lett.* 225 (2018) 13–16.
- [56] S.A. Khairallah, A.T. Anderson, A. Rubenchik, W.E. King, Laser powder-bed fusion additive manufacturing: Physics of complex melt flow and formation mechanisms of pores, spatter, and denudation zones, *Acta Mater.* 108 (2016) 36–45.
- [57] D.H. StJohn, M. Qian, M.A. Easton, P. Cao, The Interdependence Theory: The relationship between grain formation and nucleant selection, *Acta Mater.* 59 (12) (2011) 4907–4921.
- [58] M.A. Easton, D.H. StJohn, Improved prediction of the grain size of aluminum alloys that includes the effect of cooling rate, *Mater. Sci. Eng.: A* 486 (1-2) (2008) 8–13.
- [59] K. Zhang, X. Tian, M. Bermingham, J. Rao, Q. Jia, Y. Zhu, A. Huang, Effects of B addition on microstructures and mechanical properties of Ti-6Al-4V manufactured by direct laser deposition, *Mater. Des.* 184 (2019) 108191.
- [60] Z. Zhou, Y. Liu, New insights into the evolution of TiB whisker and TiC particle during selective laser melting of titanium matrix composites, *Mater. Sci. Eng.: A* (2023) 145200.
- [61] F.J. Gil, M.P. Ginebra, J.M. Manero, J.A. Planell, Formation of α -Widmanstätten structure: effects of grain size and cooling rate on the Widmanstätten morphologies and on the mechanical properties in Ti-6Al-4V alloy, *J. Alloy. Compd.* 329 (1-2) (2001) 142–152.
- [62] D. Brodtkin, M.W. Barsoum, Isothermal Section of Ti-B-C Phase Diagram at 1600° C, *J. Am. Ceram. Soc.* 79 (3) (1996) 785–787.
- [63] Z. Ye, X. Zhou, F. Zhang, K. Wang, K. Zhao, Z. Yu, H. Tan, Effects of process parameters on the microstructure and mechanical properties of a laser micro-alloying TiB/Ti-6Al-4V titanium matrix composite, *Mater. Sci. Eng.: A* 873 (2023) 144988.
- [64] M. Chen, M. Simonelli, S. Van Petegem, Y.Y. Tse, C.S.T. Chang, M.G. Makowska, H. Moens-Van Swygenhoven, A quantitative study of thermal cycling along the build direction of Ti-6Al-4V produced by laser powder bed fusion, *Mater. Des.* 225 (2023) 111458.
- [65] E.W. Lui, W. Xu, A. Pateras, M. Qian, M. Brandt, New development in selective laser melting of Ti-6Al-4V: a wider processing window for the achievement of fully lamellar α + β microstructures, *Jom* 69 (2017) 2679–2683.